HAL open science

Nonclassical Nucleation and Crystallization of LiNbO 3 Nanoparticles from the Aqueous Solvothermal Alkoxide Route

Florian Riporto, Ameni Dhouib, Adrian Gheata, Sandrine Beauquis, Emilie Molina, Simon Guené-Girard, Christine Galez, Aurélien Bornet, Isabelle Gautier-Luneau, Sandrine Gerber-Lemaire, et al.

To cite this version:

Florian Riporto, Ameni Dhouib, Adrian Gheata, Sandrine Beauquis, Emilie Molina, et al.. Nonclassical Nucleation and Crystallization of LiNbO 3 Nanoparticles from the Aqueous Solvothermal Alkoxide Route. Small, 2023, 20 (13), pp.2306417. 10.1002/smll.202306417 . hal-04290072

HAL Id: hal-04290072

https://hal.science/hal-04290072v1

Submitted on 16 Nov 2023

HAL is a multi-disciplinary open access archive for the deposit and dissemination of scientific research documents, whether they are published or not. The documents may come from teaching and research institutions in France or abroad, or from public or private research centers.

L'archive ouverte pluridisciplinaire **HAL**, est destinée au dépôt et à la diffusion de documents scientifiques de niveau recherche, publiés ou non, émanant des établissements d'enseignement et de recherche français ou étrangers, des laboratoires publics ou privés.

Distributed under a Creative Commons Attribution - NonCommercial 4.0 International License

Check for updates

NANO · MICRO small
www.small-journal.com

Nonclassical Nucleation and Crystallization of $LiNbO_3$ Nanoparticles from the Aqueous Solvothermal Alkoxide Route

*Florian Riporto, Ameni Dhouib, Adrian Gheata, Sandrine Beauquis, Emilie Molina, Simon Guené-Girard, Christine Galez, Aurélien Bornet, Isabelle Gautier-Luneau, Sandrine Gerber-Lemaire, Virginie Monnier, Ronan Le Dantec, and Yannick Mugnier**

The exact molecular reaction pathway and crystallization mechanisms of $LiNbO_3$ nanoparticles under solvothermal conditions are derived through extensive time- and temperature-resolved experiments allowing to track all the transient molecular and solid species. Starting with a simple mixing of Li/Nb ethoxides, water addition is used to promote condensation after ligand exchange with different co-solvents including alcohols and glycols of variable carbon-chain length. A nonclassical nucleation scheme is first demonstrated after the identification of new octanuclear complexes with a $\{Li_4Nb_4O_{10}\}$ core whose solvophobic interactions mediate their aggregation, thus, resulting in a colloidal gel at room-temperature. Upon heating, a more or less frustrated aggregation-mediated crystallization process is then evidenced leading to $LiNbO_3$ nanocrystals of adjustable mean size between 20 and 100 nm. Such a fine control can be attributed to the variable Nb—OR (R = alkoxy/glycoxy ligand) binding interactions at the surface of crystalline intermediates. Demonstration of such a nonclassical nucleation process and crystallization mechanism for $LiNbO_3$ not only sheds light on the entire growth process of multifunctional nanomaterials with non-perovskite crystalline structures, but also opens new avenues for the identification of novel bimetallic oxoclusters involved in the formation of several mixed oxides from the aqueous alkoxide route.

1. Introduction

Solution-based methods leading to the preparation and rational design of advanced nanomaterials have recently witnessed a series of breakthroughs toward a better understanding of the nucleation, crystallization, and growth of several classes of materials including metals,[1] simple binary oxides,[2,3] bimetallic oxides,[4] and semiconductor quantum dots.[5] Direct experimental probing of the nanoscale dynamics, molecular reaction pathways, crystallization, and growth mechanisms through extensive in situ and real-time measurements (allowing identification of the possible transient monomers, pre-nucleation species, and primary solid intermediates) indeed demonstrate that for several wet-chemical routes, formation of nanoparticles cannot be described by classical nucleation theory and growth from monomer-by-monomer addition.[6,7] Instead, nonclassical nucleation and crystallization may involve the appearance and assembly of oxoclusters,

F. Riporto, A. Dhouib, S. Beauquis, E. Molina, C. Galez, R. Le Dantec, Y. Mugnier
Université Savoie Mont Blanc
SYMME
Annecy F-74000, France
E-mail: yannick.mugnier@univ-smb.fr

A. Gheata, S. Gerber-Lemaire
Institute of Chemical Sciences and Engineering
Ecole Polytechnique Fédérale de Lausanne
Group for Functionalized Biomaterials
Lausanne 1015, Switzerland

S. Guené-Girard, I. Gautier-Luneau
Université Grenoble Alpes
CNRS, Grenoble INP
Institut Néel
Grenoble 38000, France

A. Bornet
Institute of Chemical Sciences and Engineering
Ecole Polytechnique Fédérale de Lausanne
Nuclear Magnetic Resonance Platform
EPFL SB ISIC-NMRP
Batochime, Lausanne 1015, Switzerland

V. Monnier
Univ Lyon, Ecole Centrale de Lyon
CNRS, INSA Lyon
Université Claude Bernard Lyon 1
CPE Lyon, CNRS, INL
UMR5270, Ecully 69130, France

The ORCID identification number(s) for the author(s) of this article can be found under https://doi.org/10.1002/smll.202306417

© 2023 The Authors. Small published by Wiley-VCH GmbH. This is an open access article under the terms of the Creative Commons Attribution-NonCommercial License, which permits use, distribution and reproduction in any medium, provided the original work is properly cited and is not used for commercial purposes.

DOI: 10.1002/smll.202306417

formation of amorphous nuclei, and aggregation-induced crystallization. Similarly, the growth mechanisms are not only attributed to the traditional surface addition of ions/atoms, dissolution-precipitation phenomena (Ostwald ripening), coarsening of crystalline intermediates, and oriented attachment.[8] Growth from primary nanocrystals may also proceed from the attachment of molecules, clusters, amorphous intermediates, or non-oriented nanocrystals and subsequent recrystallization.[6] Noteworthy, organic binding moieties within molecular precursors/monomers and organic–inorganic interactions between ligands and primary solid intermediates are also known to play a crucial role in the overall formation and crystallization mechanisms.[2,3,6,7,9,10]

Regarding the synthesis of noncentrosymmetric oxides (NCO), i.e., of multifunctional nanomaterials exhibiting structure-induced properties, such as ferroelectricity, pyroelectricity, piezoelectricity, and second harmonic generation, solution-based routes have also proven their efficiency in the reproducible preparation of several, representative crystalline hosts, such as $BaTiO_3$ and its derivatives, multiferroic $BiFeO_3$, $KTiOPO_4$, and niobate ($K/Na/LiNbO_3$) or iodate compounds.[11] Because of a much higher complexity in terms of compositions (such as ternary, quaternary and even quinary oxides) and crystal structures belonging to lower symmetry point groups, trapping the "randomness of the solution state"[12,13] is also for NCO nanocrystals an appealing approach to obtain the desired stoichiometry. Note that use of preformed stoichiometric moieties already containing oxobridges between different metal cations is another source of inspiration.[11,14] However, contrary to centrosymmetric nanomaterials, the exact derivation of the reaction pathways and crystallization mechanisms is less straightforward and still needs the special attention of the research community for improving the resulting performances of NCO nanocrystals in the near future. Among the multifunctional oxide nanocrystals produced at the nanoscale from the alkoxide route under mild solvothermal conditions, lithium niobate ($LiNbO_3$, denoted here as LN) is an illustrative example of a reference optical material for which the formation mechanisms, starting from the molecular to the crystallization and growth levels, are still barely understood. In comparison to other wet-chemical approaches, a key feature of the solution-mediated synthesis of NCOs under solvothermal conditions is the more likely formation of crystalline nanomaterials without subsequent high-temperature annealing treatment systematically leading to a higher degree of aggregation state.[15,16] In the pioneering work of Niederberger et al., flattened LN nanocrystals in the 20–50 nm size range were thus obtained from $Nb(OEt)_5$ and metal Li dissolved in benzyl alcohol after 4 d of treatment at 220 °C.[17] Following this proof-of-principle study, typical experimental conditions involve niobium ethoxide in benzyl alcohol, 3 or 4 d of solvothermal treatments at 220–230 °C, and surfactants as recently demonstrated by the group of Gates.[18–21] Interestingly, at a very low hydrolysis rate of the reaction medium when $LiOH{\cdot}H_2O$ is used as the lithium source, agglomeration of ≈5 nm poorly ordered LN crystalline intermediates was proposed to account for the initial formation of $LiNbO_3$ whereas Ostwald ripening and aggregation mediate the final growth of LN nanocrystals. Hydrolysis of the niobium ethoxide precursor was believed to result in $NbO_x(OH)_y(OR)_z$ species either after water addition[18,21] or from solvolysis under non-aqueous conditions,[19] as such sol–gel precursors were expected before condensation can occur. Because identification of the molecular species and byproducts in the reaction medium was not established, the exact molecular reaction pathway is still to be determined. Indeed, the influence of the Li source, for instance, has a huge effect on the morphology, purity, and crystallinity of the final $LiNbO_3$ products.[20] On the other hand, almost spherical and cubic-like LN nanocrystals were also prepared from a commercial double ethoxide precursor ($LiNb(OEt)_6$) diluted in its parent alcohol and with different amounts of 1,4-butanediol[22] following the ligand exchange strategy suggested by Livage and co-workers for transition metal oxides.[23,24] For this non-aqueous route and after a systematic variation of the chain length R of different glycols used as co-solvent, sub-50 nm $LiNbO_3$ nanocrystals of adjustable mean size and shape anisotropy were also produced in our group.[25] The proposed reaction pathway involves ligand exchange with the initial double ethoxide, thermal dissociation of the modified precursor leading to $[NbO(OR)_4]^-$ ions and to positively charged carbocations whose stability directly influences the formation rate of the $Li[NbO(OR)_4]$ monomers and the precipitation of smaller nanocrystals when long carbon-chain glycols are used as co-solvents. After nucleation, a classical growth mechanism is assumed after addition, by a nucleophilic attack, of the remaining monomers. The final nanocrystal shape anisotropy was attributed to the pseudoilmenite crystalline structure of $LiNbO_3$ and to the presence of different surface ethoxy/glycoxy groups along the polar direction of the growing nanocrystals.[25]

In terms of potential applications, adjustment of the final LN nanocrystal size in a broader range and preparation of colloidal suspensions in water or ethanol for further chemical surface modification is mainly driven by recent proof-of-concept studies in the nanomedicine field. Bio-related applications of LN nanoparticles as well as other NCO nanocrystals have indeed been the subject of increasing research interest over the last decade, primarily in terms of exogenous contrast agents.[26,27] Their reduced dimensions below 100 nm indeed remarkably come into play since the scattering of multiple nonlinear optical signals is no longer hindered by the severe constraint of phase-matching conditions.[28,29] Their extremely rich non-linear optical properties, long-term photo-stability,[30] and excitation-wavelength tunability for deep imaging[31] have thus paved the way for these new advances in the bio-imaging field, especially for very long-term and fast in vivo acquisitions in the NIR transparency windows.[29,32–34] In parallel, proper surface functionalization of LN nanocrystals has recently allowed an increase of their multifunctionality in terms of fluorescence imaging,[35] of dual multiphoton and MRI contrast agents[36] and for the local on-demand release of chemotherapeutics.[37,38]

In this study, aqueous conditions with a low hydrolysis rate h fixed at 1.5 (h is here defined as the ratio between the number of water molecules and of precursor ethoxy groups), are investigated with the aim to promote at room temperature the condensation of primary solid species and to shorten the total solvothermal reaction time to only 1 d at 235 °C. After the addition of water, qualitative dynamic light scattering (DLS) measurements coupled with mass spectroscopy and NMR measurements first allow better identification of the transient molecular species, namely oxoclusters, leading at room temperature through a nonclassical

© 2023 The Authors. Small published by Wiley-VCH GmbH

16136829, 0, Downloaded from https://onlinelibrary.wiley.com/doi/10.1002/smll.202306417 by Cochrane France, Wiley Online Library on [15/11/2023]. See the Terms and Conditions (https://onlinelibrary.wiley.com/terms-and-conditions) on Wiley Online Library for rules of use; OA articles are governed by the applicable Creative Commons License

nucleation scheme, to a colloidal gel composed of ≈5 nm amorphous nuclei as demonstrated from SAXS data and Transmission electron microscopy (TEM) imaging. Kinetics of the gel formation is directly mediated by the solvophobic interactions of the oxocluster pendant chains after ligand exchange of the lithium niobium ethoxy groups with longer alkoxy/glycoxy groups provided by a large variety of co-solvents including several primary and secondary alcohols of different carbon-chain lengths and various glycols. Time- and temperature-resolved solvothermal treatments demonstrate an aggregation-mediated crystallization mechanism leading to LN nanocrystals of adjustable mean size and anisotropy. Solvophobic interactions between the polar solvent and the surface alkoxy/glycoxy groups of solid crystalline intermediates promote their agglomeration upon heating resulting in monolith formation within the autoclave after the solvothermal treatment. Inductive effects of the surface carbon chains also mediate the core-ligand binding interactions and the mesoscale transformation within the primary hybrid aggregates[10] after rearrangement of the organic layer. Low binding interactions associated with strong inductive effects are shown to result in smaller hybrid aggregates and LN nanocrystals whereas weak inductive effects both frustrate the removal of the surface-anchored ligands and crystallization of $LiNbO_3$, thus increasing the final nanoparticle size.

2. Results

2.1. Molecular Reaction Pathway and Gel Formation Upon Hydrolysis

Qualitative FTIR studies of the separate precursors and their mixing were first conducted with the aim to attest their purity and to avoid any significant contribution of toluene as we recently observed from several commercial, bimetallic lithium niobium ethoxide sources.[25] Toluene is indeed used in the alkoxide preparation to remove water through azeotropic distillation. The dimeric nature of non-diluted niobium ethoxide, $Nb_2(OEt)_{10}$, has already been demonstrated from FTIR[39] and NMR[40,41] spectroscopies allowing clear identification of the terminal and bridging ethoxy groups. Accordingly, the FTIR spectrum of pure niobium ethoxide (Figure S1a, Supporting Information) evidences a double peak at 560–580 cm^{-1} originating from the elongation and angular deformation of the Nb−O bonds and two characteristic C−O vibrations at 878 and 909 cm^{-1} (symmetric stretching) for the bridging and terminal ethoxy groups, respectively. After dilution in ethanol, the relative intensity at 878 cm^{-1} (and to a less extent at 1028 cm^{-1} for the asymmetric stretching of C−O in the bridging group) is strongly reduced in agreement with a decrease of the molecular complexity of niobium ethoxide from 2 to 1.52.[42] Upon mixing of the two precursors, the formation of the bimetallic alkoxide $LiNb(OCH_2CH_3)_6$ is attested by the absence of the two characteristic C−O vibrations at 878 and 1028 cm^{-1} (Figure S1b, Supporting information). A shift to lower frequencies of the C−O vibrations of the remaining terminal ethoxy groups is also observed at 1101 and 897 cm^{-1} due to the higher reduced mass of the bimetallic compound. They are attributed to the asymmetric and symmetric stretching of C−O, respectively, while the band at 1058 cm^{-1} can be assigned to the CH_3 in-plane rocking mode.[43] Schematic evolution of the niobium ethoxide precursor after dilution in ethanol and the addition of lithium ethoxide is illustrated in Figure S1c (Supporting Information) as already evidenced by Eichorst et al. from ^{13}C NMR spectroscopy.[40] Here, the ^{93}Nb spectra depicted in Figure S1d (Supporting Information) also demonstrate a huge change from a mixture of Nb monomers and dimers[42] for the $Nb(OEt)_5$ solution diluted in ethanol and after the addition of Li(OEt).

Before the addition of water to promote condensation at room temperature, the high reactivity of metal alkoxides toward moisture is to be considered. Ligand exchange with longer alkyl chains was, for instance, necessary to avoid precipitation at a low hydrolysis rate of $Nb(OCH_2CH_3)_5$ and for the preparation of stable sols and gels before their calcination into niobium pentoxide powders.[44] Ligand exchange, as also discussed in Section 2.3, was here investigated from ^7Li NMR spectroscopy after the addition of an excess of various co-solvents including alcohols and glycols. As an example, Figure S1e (Supporting Information) highlights the ^7Li spectra of lithium niobium ethoxide in its parent alcohol and after the addition of 1,4-butanediol. The resulting peak shift and broadening are associated with the formation of bulkier moieties while the single peak, observed for the Li resonance in both cases, is consistent with a single chemical environment. Probing molecular transformation of the bimetallic $LiNb(OEt)_6$ monomer (or of $LiNb(OR)_6$ after ligand exchange) upon hydrolysis was then qualitatively monitored from standard DLS measurements although real-time size measurements were not tested as in the pioneering work of Kanaev and co-workers dedicated to Ti-based oxoclusters.[45] Here, the DLS size distribution, in volume, of the bimetallic precursor at 0.133 M in its parent alcohol evidences a peak centered at ≈1 nm in good agreement with the size of the proposed $[LiNb(OEt)_8]^{2-}$ molecular entities present in solution (Figure S2, Supporting Information). Note that a diameter at 0.96 nm can also be derived from the volume of the orthorhombic cell of $LiNb(OEt)_6$ crystals containing 16 formulae units.[46] After water addition, the size distribution in volume was immediately acquired for a low hydrolysis rate fixed at 0.5 (to keep the reaction medium viscosity constant), resulting in a size increase to ≈3 nm. Similarly, gel formation was purposely prevented by decreasing the initial precursor concentration in ethanol by a factor of 10. A peak centered in the 2.5–3.5 nm size range was then obtained for a hydrolysis rate fixed at 1.5 and when butanol and heptanol are for instance used as co-solvents. In each case, the reaction medium was still transparent after the DLS measurement and no change in the viscosity could be observed.

Accurate MS experiments were then conducted in the positive mode by nanochip-ESI to probe the potential formation of a double metal alkoxide of Li since a few have already been identified[47] and especially $[LiNbO(OEt)_4EtOH]_2$ of molecular mass ≈684 Da.[48] A comparison of the ESI mass spectra before and after hydrolysis of the precursor solution is given in **Figure 1**a. Upon water addition at $h = 0.5$ for 5 min to prevent any gel formation, several peaks appear in the blue-shaded "high-mass" region corresponding to the 1110–1300 Da range. After implementation of simple calculations based on the electroneutrality and possible chemical composition of the as-obtained molecular species (see Figure S3, Supporting Information), these peaks were all attributed to a newly evidenced octanuclear

© 2023 The Authors. Small published by Wiley-VCH GmbH

16136829, 0, Downloaded from https://onlinelibrary.wiley.com/doi/10.1002/smll.202306417 by Cochrane France, Wiley Online Library on [15/11/2023]. See the Terms and Conditions (https://onlinelibrary.wiley.com/terms-and-conditions) on Wiley Online Library for rules of use; OA articles are governed by the applicable Creative Commons License

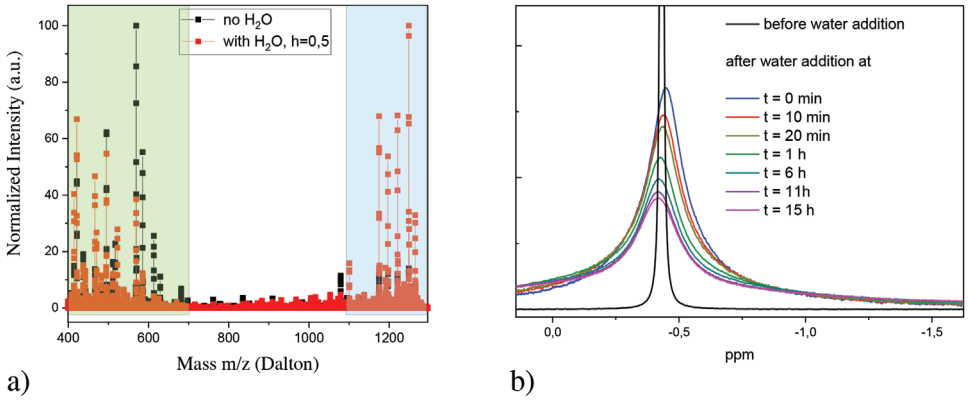

Figure 1. a) Nanochip-ESI MS of the precursor solution before and after water addition at $h = 0.5$ leading to several new peaks above 1180 Da in the so-called "high-mass" region (1110–1300 Da, blue-shaded). In the "low-mass" green-shaded region (400–700 Da) main peaks are all attributed to cationic species deriving from the tetranuclear complex $[LiNbO(OEt)_4EtOH]_2$ whereas, in the "high-mass" region, peaks resulting from the water addition can be assigned to cationic species arising from $[Li_4Nb_4O_{10}(OEt)_4(EtOH)_{12}]$ oxoclusters. b) Time-resolved ^{7}Li NMR spectra indicating the immediate formation of oxoclusters after hydrolysis has been initiated at $h = 0.5$.

complex of composition $[Li_4Nb_4O_{10}(OEt)_4(EtOH)_{12}]$. Interestingly, in the green-shaded "low-mass" region (400–700 Da) of Figure 1a, a significant decrease of the peaks deriving from the bimetallic tetranuclear alkoxide $[LiNbO(OEt)_4EtOH]_2$ can also be assigned to several cationic species after exchange of EtO^- groups with HO^- ions and partial fragmentation.

Formation of bulkier moieties corresponding to mixed octanuclear complex, $[Li_4Nb_4O_{10}(OEt)_4(EtOH)_{12}]$, with a $\{Li_4Nb_4O_{10}\}$ core unit, is also evidenced from ^{7}Li NMR spectroscopy for a low hydrolysis rate fixed at $h = 0.5$. Kinetics measurements plotted in Figure 1b at different time intervals after water addition indeed demonstrate an instantaneous shift and broadening of the Li resonance without noticeable change in the reaction medium viscosity for 15 h. A significant decrease in the diffusion coefficient is also monitored from DOSY experiments (Figure S4a, Supporting Information). They were conducted before and just after hydrolysis has started, i.e., once the oxoclusters are produced from the $LiNb(OEt)_6$ monomer. Finally, after 6 h, the additional shoulder measured at ≈−1.7 ppm (Figure S4b,c, Supporting Information) may indicate that larger structures are already present, presumably the first amorphous nuclei.

Regarding the gelation time for the standard experimental conditions, namely 4.5 mL of $LiNb(OCH_2CH_3)_6$ at 0.133 M in ethanol and 2.25 mL of co-solvent, the addition of water corresponding to $h = 1.5$ leads to variable change of the reaction medium. For simple alcohols, the longer the carbon chain, the shorter the formation of translucent gels as it can be visually observed 10 min after hydrolysis has been initiated (Figure S5, Supporting Information). This again demonstrates the ligand exchange since the variable solvophobic interactions of the oxocluster pendant chains are responsible for the colloidal gel formation upon aging at room temperature under magnetic stirring. Inversely, for glycols, the reaction medium remains transparent for 24 h when 1,3-propanediol is for instance used as the co-solvent in agreement with lower solvophobic interactions within the polar medium due to the terminal OH of the glycoxy group. For the other glycols whose carbon-chain length is gradually increased from 1,4-butanediol to 1,7-heptanediol, the appearance of the gel is typically observed after a few hours to several minutes, respectively.

To get further insight into the properties of the as-produced gel, SAXS measurements were conducted either after drying under vacuum when ethanol was the only solvent (**Figure 2**; Figure S6, Supporting Information, for the gel evolution at room temperature for 4 d) or with several glycols (Figure S7, Supporting Information, in the case of 1,5-pentanediol) after 4 d at ambient pressure to allow syneresis and partial removal of the solvent mixture. This leads to higher signal-to-noise ratios due to a larger number of solid species within the mylar sheets. The SAXS data were then fitted with a form factor describing polydisperse spheres leading to a core size of ≈4 nm associated with a large polydispersity at 30–40%. X-ray diffraction confirms that condensation of the oxoclusters leads to amorphous nuclei at room temperature. These latter do not show any significant evolution after a solvothermal treatment of 24 h at 100 or 150 °C as illustrated in the TEM images featuring loosely packed nuclei with typical dimensions below 5–6 nm (Figure 2b,c; Figure S7b, Supporting Information, see also Section 2.3 for the temperature-resolved studies).

2.2. Influence of the Co-Solvent on the Resulting Nanocrystal Size

With the aim to derive the exact crystallization mechanism and to possibly control the final nanocrystal morphology in a broad range of sizes, solvothermal treatments of the gels prepared at room temperature with different co-solvents were conducted for 24 h at 235 °C. The addition of a fixed volume (2.25 mL) of co-solvent to the initial 4.5 mL of $LiNb(OCH_2CH_3)_6$ at 0.133 M in ethanol has several effects. First, the molar concentration of each co-solvent is different because of its own molar mass. The overall physicochemical properties of the reaction medium are also varied. A change in the permittivity and viscosity of a co-solvent, for instance, has been proposed to play a crucial role in the morphology of $BaTiO_3$ nanocrystals prepared under similar solvothermal treatments.[49,50] Finally, the autogenous pressure at a given temperature is also known to strongly vary with the solvent molar volume.[51] Since the precursor concentration may also influence the final nanocrystal morphology, a first set

 © 2023 The Authors. Small published by Wiley-VCH GmbH

16136829, 0, Downloaded from https://onlinelibrary.wiley.com/doi/10.1002/smll.202306417 by Cochrane France, Wiley Online Library on [15/11/2023]. See the Terms and Conditions (https://onlinelibrary.wiley.com/terms-and-conditions) on Wiley Online Library for rules of use; OA articles are governed by the applicable Creative Commons License

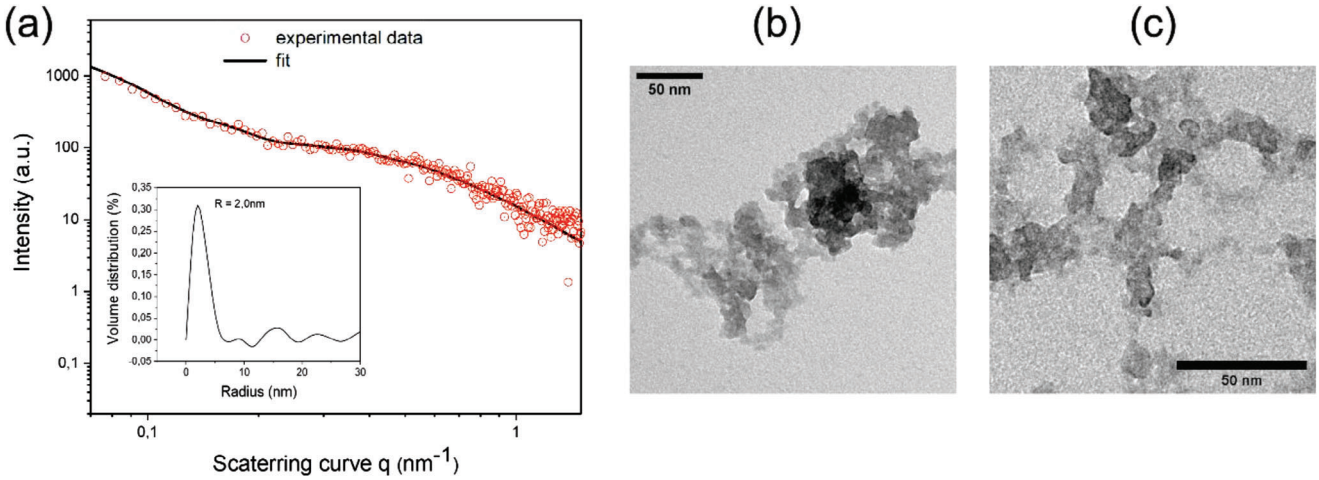

Figure 2. a) SAXS scattering curve for a gel dried under vacuum prepared at $h = 1.5$ from $LiNb(OCH_2CH_3)_6$ with ethanol as the only solvent. Inset: Corresponding volume distribution giving a core size of 4 nm with a typical polydispersity of 30–40%. b,c) Representative TEM images after a solvothermal treatment of 24 h at 100 and 150 °C, respectively, showing amorphous nuclei with typical features in the 5 nm size range.

of experiments was conducted by varying the molar ratio r defined as the molar concentration of butanol to ethanol. Addition of 1.13 mL (r = 0.15), 2.25 mL (r = 0.31), 3.38 mL (r = 0.46), and 4.51 mL (r = 0.62) of butanol to the initial precursor volume of 4.5 mL in ethanol not only result in phase pure samples but to an almost constant nanocrystal size S_{012} at ≈16–17 nm (Figure S8, Supporting Information). Note that the apparent nanocrystal size S_{hlk} estimated along each [hkl] direction is always found between the ones obtained from the (006) and (110) reflections. A flattened morphology with an anisotropic factor (defined as $f = S_{110}/S_{006}$) at about 3 is thus always obtained, showing a minimal influence of the filling fraction and autogenous pressure within the autoclave and of the precursor concentration. Conversely, the addition of 2.25 mL of primary alcohols ranging from ethanol to heptanol results in a broader range of nanocrystal size since the mean size S_{012} continuously decreases from 23 nm (when only ethanol is used) to 15 nm for the longer alcohols containing five to seven carbon atoms in the alkyl chain (**Figure 3**). The same size decrease is also observed for the (110) and (006) reflections, and the absence of any phase impurity can also be noticed by comparison with the reference ICSD pattern # 94 493 of LN. Assessment of the mean nanocrystal size from TEM observations is also provided with a supposed disk-shaped morphology. Assuming that a given size distribution is to be considered along each [hkl] direction together with various inclinations of the individual nanocrystals on the TEM grid, the histograms depicted in Figure 3c are consistent with the X-ray diffraction (XRD) refinements. The size distributions centered at 40, 35, and 24 nm corresponding to the addition of 2.25 mL of ethanol, butanol, and heptanol, respectively, evidence a similar average size reduction as long as the alkyl chain is increased (see also Figure S9, Supporting Information, for additional TEM images at higher resolution better illustrating the size and shape polydispersity). Interestingly, the location of the OH group in the alkyl chain has almost no influence on the final nanocrystal sizes derived from Le Bail refinements. A comparison between the use of primary and secondary alcohols is provided in Figure S10a,b (Supporting Information), showing similar results for alkyl chains of increasing length containing three to seven carbon atoms.

When glycols of increasing chain length are used as co-solvent, a drastic change can be observed in both the nanocrystal size and phase purity. The mean nanocrystal size S_{012} derived from XRD refinements is estimated in **Figure 4** at 74, 56, and 22 nm for 1,4-butanediol, 1,5-pentanediol, and 1,7-heptanediol, respectively. For the first two co-solvents, TEM image analysis leads to histograms with size distributions centered at 100 and 64 nm, thus confirming a substantial size increase by comparison with the use of primary or secondary alcohols of the same carbon chain length. Regarding 1,7-heptanediol, the derived nanocrystal sizes for the (012), (110), and (006) reflections are very close to the ones observed with only ethanol (see Figure S11, Supporting Information, for a direct comparison of the nanocrystal sizes obtained with the different primary alcohols and glycols). For the shortest glycol, namely 1,3-propanediol, partial crystallization of the $LiNbO_3$ phase is attested by the presence of diffraction peaks whose FWHM is similar to the instrumental resolution thus preventing any accurate estimation of the particle size from XRD refinement. More importantly, we also observe broad bands corresponding to the 6.5 Å phase previously obtained by Nyman et al. when Lindqvist ions were used as starting precursors and from hydrothermal treatments for 1 d of lithium-rich aqueous solutions.[52] Experimental XRD patterns of this transient, not yet identified phase, have also been evidenced in more recent studies.[18,21] Here, low- and high-resolution TEM images of the samples prepared with 1,3-propanediol reveal the occurrence, in agreement with the XRD pattern, of LN particle size above ≈120 nm and a larger amount of almost spherical nanocrystals at 5–8 nm (Figure S12, Supporting Information), evidencing a morphology similar to the one observed from the amorphous nuclei of the gel heat-treated at 100 and 150 °C (Figure 2b,c). In the formation of the $LiNbO_3$ phase, these crystalline intermediates (see also Section 2.3) have their largest d-spacing at 6.5 Å and may evidence in the HRTEM images a square arrangement of Nb atoms. It can be noticed that these intermediates are also visible in the TEM image of the sample prepared with 1,4-butanediol

 © 2023 The Authors. Small published by Wiley-VCH GmbH

16136829, 0, Downloaded from https://onlinelibrary.wiley.com/doi/10.1002/smll.202306417 by Cochrane France, Wiley Online Library on [15/11/2023]. See the Terms and Conditions (https://onlinelibrary.wiley.com/terms-and-conditions) on Wiley Online Library for rules of use; OA articles are governed by the applicable Creative Commons License

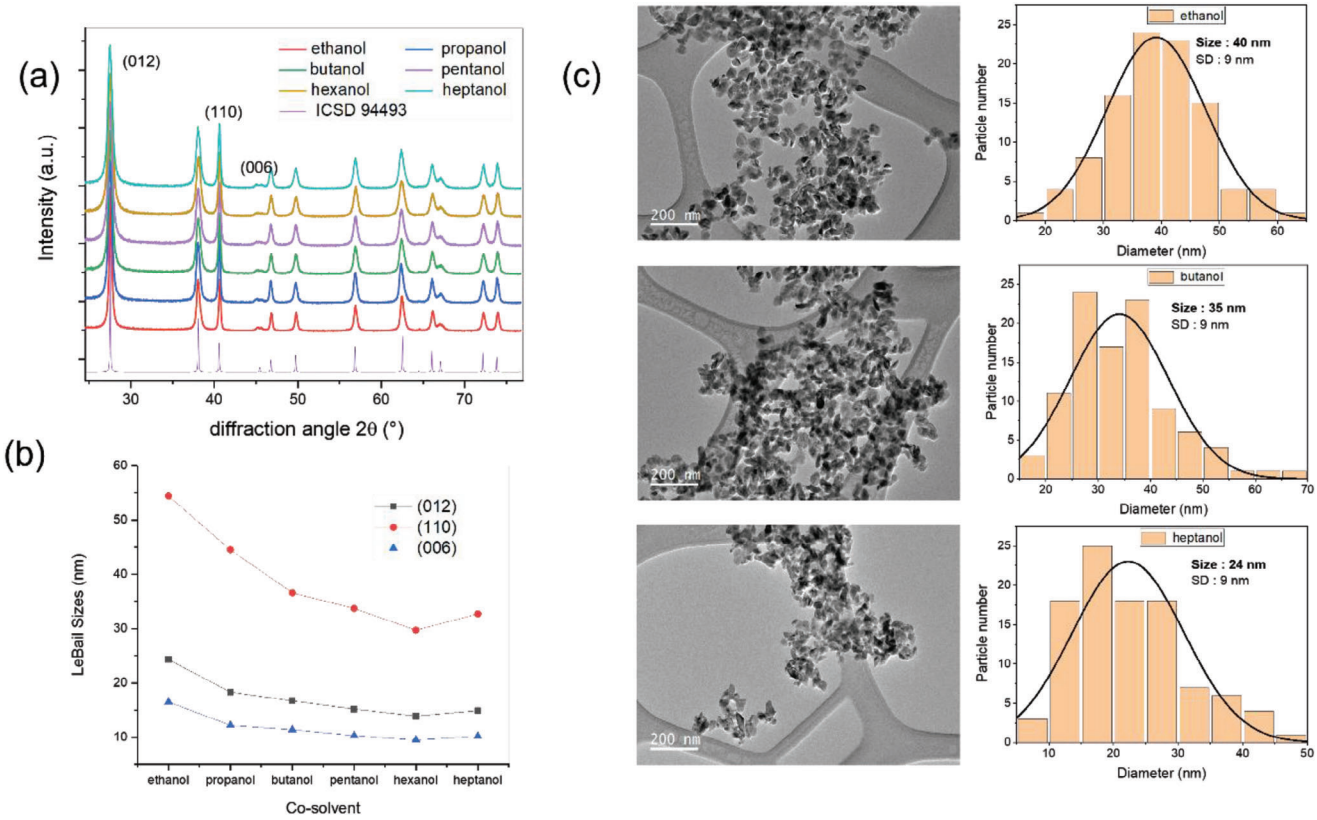

Figure 3. a) XRD diffraction patterns of LN nanocrystals produced at $h = 1.5$ with 2.25 mL of co-solvent of increasing chain length ranging from ethanol to heptanol. b) Corresponding nanocrystal sizes derived from the (012), (110), and (006) reflections after refinement of the XRD profiles with the Le Bail fitting procedure. c) Representative TEM images and associated size distribution histograms for the ethanol, butanol, and heptanol cases showing a reduction of the average particle size for a constant standard deviation at ≈9 nm.

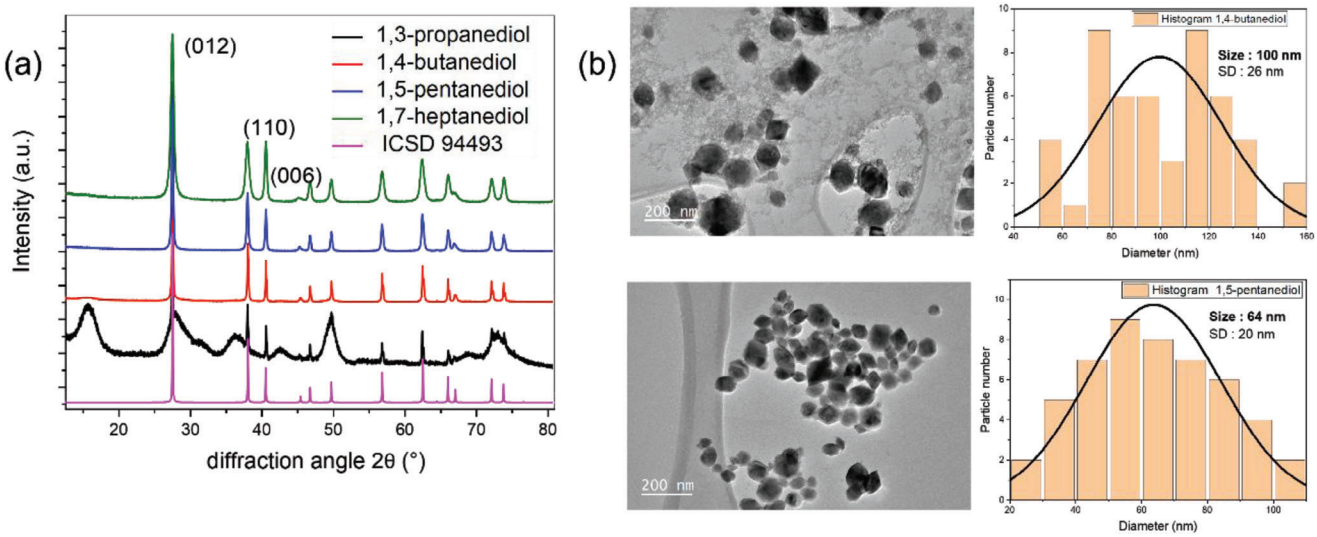

Figure 4. a) XRD diffraction patterns of LN nanocrystals produced at $h = 1.5$ with 2.25 mL of glycols of increasing chain length ranging from 1,3-propanediol to 1,7-heptanediol. b) Representative TEM images and associated size distribution histograms for samples prepared with 1,4-butanediol and 1,5-pentanediol.

 © 2023 The Authors. Small published by Wiley-VCH GmbH

16136829, 0, Downloaded from https://onlinelibrary.wiley.com/doi/10.1002/smll.202306417 by Cochrane France, Wiley Online Library on [15/11/2023]. See the Terms and Conditions (https://onlinelibrary.wiley.com/terms-and-conditions) on Wiley Online Library for rules of use; OA articles are governed by the applicable Creative Commons License

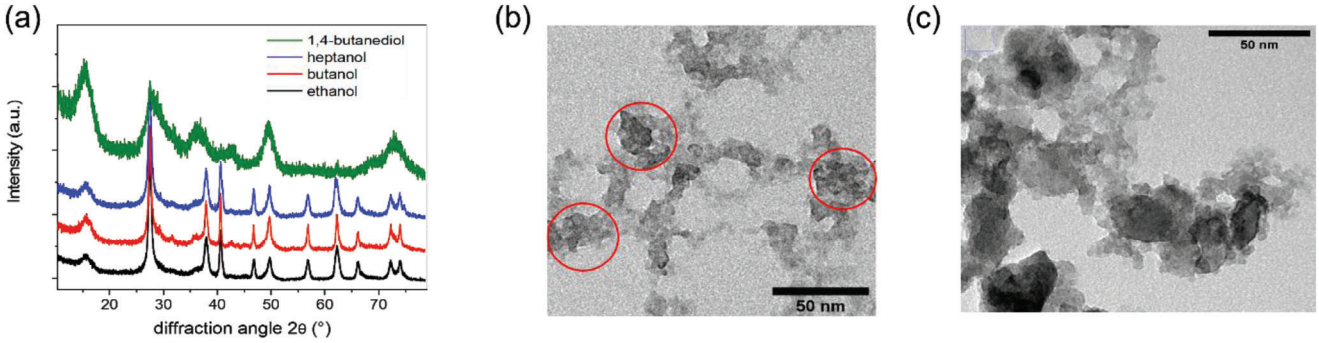

Figure 5. a) XRD diffraction patterns of samples produced at $h = 1.5$ with 2.25 mL of co-solvent including ethanol, butanol, heptanol, and 1,4-butanediol. The influence of the alkoxy/glycoxy chain on the purity and crystalline degree of LN is shown after a solvothermal treatment of 24 h at 200 °C. Corresponding TEM images of the sample prepared with only ethanol at 150 °C (b) and 200 °C (c), respectively show agglomerates of the amorphous transient species (red circles) and primary LN nanocrystals surrounded by the crystalline intermediates.

(Figure 4b) but their small size and lower concentration, in comparison with the 1,3-propanediol case, make them difficult to be detected by XRD.

Additional electron microscopy data are provided in Figures S13 and S14 (Supporting Information). For LN nanocrystals, HRTEM imaging demonstrates the expected pseudosquare arrangement of Nb atoms in the equivalent (012), (1-12), and (−102) planes with a 3.77 Å spatial separation whereas Selected Area Electron Diffraction (SAED) patterns result in d-spacings corresponding to the most intense diffraction peaks of the $LiNbO_3$ phase. For the crystalline intermediates, SAED patterns also lead to reticular distances that are consistent with the 6.5 Å phase already discussed. Because of the crystallite size at 5–8 nm and associated peak broadening, our first attempts to identify a definitive lattice system and possible crystalline structure were inconclusive but work is in progress to derive the exact chemical composition and to stabilize larger crystallites. Noteworthy, hydrothermal synthesis of niobate compounds is known to result in several transient phases and still unidentified polyoxoniobate phases despite careful examination of the available structures in the crystallography databases.[53] In the following section, the influence of the co-solvent and thermal stability of these crystalline intermediates are further studied to elucidate the crystallization mechanisms of the $LiNbO_3$ phase.

2.3. Temperature- and Time-Resolved Solvothermal Treatments

The effect of the temperature treatment is illustrated in **Figure 5**a after the addition of 2.25 mL of ethanol, butanol, heptanol, and 1,4-butanediol at $h = 1.5$ and for a solvothermal treatment of 24 h at 200 °C. For the three primary alcohols, diffraction patterns evidence the presence of the 6.5 Å phase together with the formation of primary LN nanocrystals. At lower processing temperatures, namely 100 and 150 °C, and for all the tested co-solvents, only amorphous solid species were obtained after 24 h as depicted in Figure S15 (Supporting Information) for the heptanol case. Corresponding TEM images of the samples prepared at 150 and 200 °C with only ethanol (Figure 5b,c) then demonstrate sub-50 nm loosely packed agglomerates of the 5–6 nm transient species and primary LN nanocrystals surrounded by the remaining crystalline intermediates of the 6.5 Å phase, respectively. Regarding 1,4-butanediol and similarly to the 1,3-propanediol case at 235 °C, crystallization of the $LiNbO_3$ phase is also frustrated after 24 h at 200 °C, presumably due to higher binding interactions of the glycoxy groups at the surface of the crystalline intermediates. Note that surface organic ligands of the transient amorphous and crystalline species are also readily detected from EDS spectroscopy, for instance with heptanol as the co-solvent for a sample produced at $h = 1.5$ and 150 °C for 24 h (Figure S16, Supporting Information). When crystallization of $LiNbO_3$ is fully achieved with 1,4-butanediol, i.e., for instance after 48 h at 235 °C, the absence of the crystalline intermediates can be noticed from TEM imaging whereas EDS measurements demonstrate a net decrease of the carbon contribution and the expected weight fraction of O and Nb at 33% and 67%, respectively (Figure S17, Supporting Information).

Altogether, the above experimental results dealing with the various gelation times associated with the different solvophobic interactions of the oxocluster alkoxy/glycoxy groups and the minimum crystallization temperature of the LN phase indicate a key role of the surface organic binding moieties during the overall formation mechanism of $LiNbO_3$ nanocrystals. Time-resolved experiments including XRD/FTIR measurements and TEM imaging of the samples prepared at a processing temperature of 235 °C were then conducted at different durations fixed at 3, 6, 9, and 12 h. XRD patterns acquired from samples produced at $h = 1.5$ with 2.25 mL of 1,4-butanediol demonstrate the only formation of the 6.5 Å transient species after 3 h and, in **Figure 6**a, its progressive transformation to the $LiNbO_3$ phase for longer treatments. After 12 h, the contribution of the crystalline intermediates is barely detectable from XRD. Corresponding TEM images evidence large and densely-packed agglomerates of ≈50–100 nm size composed of the transient 6.5 Å species, especially after 3 and 6 h of solvothermal treatment (Figures 6b,c). Similar time-resolved experiments, using 1,5-pentanediol as the co-solvent, led to the exact same sequences in the crystallization pathway (Figure S18, Supporting Information, for the corresponding XRD patterns and TEM images) and also to the early formation of sub-100 nm dense agglomerates. After 9 and 12 h, low magnification TEM images show that these agglomerates are still present but faceted and large LN nanocrystals at ≈80 nm are also detected (Figure 6d,e; Figure S18d,e, Supporting Information). HRTEM images reveal as well that primary LN nanocrystals produced

 © 2023 The Authors. Small published by Wiley-VCH GmbH

16136829, 0, Downloaded from https://onlinelibrary.wiley.com/doi/10.1002/smll.202306417 by Cochrane France, Wiley Online Library on [15/11/2023]. See the Terms and Conditions (https://onlinelibrary.wiley.com/terms-and-conditions) on Wiley Online Library for rules of use; OA articles are governed by the applicable Creative Commons License

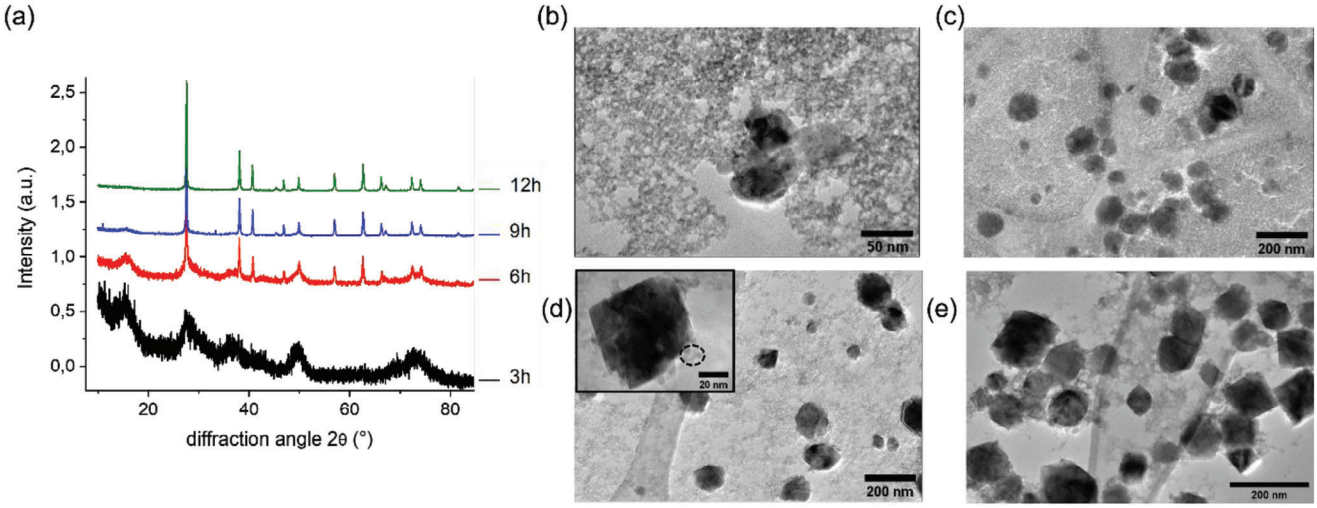

Figure 6. a) Time-resolved XRD diffraction patterns of samples produced at $h = 1.5$ with 2.25 mL of 1,4-butanediol and corresponding TEM images after a solvothermal treatment at 235 °C for 3 h (b), 6 h (c), 9 h (d), and 12 h (e). Note that XRD patterns obtained after 6 h, 9 h, and 12 h are normalized to the intensity of the highest peak corresponding to the (012) reflection of LN.

after 9 or 12 h are decorated with the remaining, surface-attached crystalline intermediates (see Figure S19, Supporting Information, for the enlarged insets of Figure 6d; Figure S16e, Supporting Information, corresponding to the two glycols tested).

Regarding the use of primary alcohols and the easier formation of the $LiNbO_3$ phase already observed in Figure 5 after 24 h at 200 °C, time-resolved experiments conducted with ethanol, butanol, and heptanol resulted in very similar trends. They are illustrated in Figure S20 (Supporting Information) for the ethanol case and first highlight a weaker content of the crystalline intermediates after 3 h but the same time-dependent sequence of phase transformation with an increase of the $LiNbO_3$ content at the expense of the 6.5 Å transient phase. After 12 h, HRTEM imaging and associated FFT treatments (Figure S20e–h, Supporting Information) also evidence that at the later stages of the crystallization process of LN, attachment and recrystallization of the remaining crystalline intermediates are involved at the surface of the primary LN nanocrystals. Similarly to the use of glycols as co-solvent (Figure 6), TEM images are consistent with the XRD patterns but show with primary alcohols a faster transformation into LN from the aggregated crystalline intermediates. Because of the various final nanocrystal sizes observed from all the tested alcohols and glycols, and different kinetics of formation of the $LiNbO_3$ phase, detailed FTIR analyses were conducted to get a better insight into the surface composition of all the solid species involved in the crystallization of LN. They are illustrated in Figure S21 (Supporting Information) with 1,5-pentanediol as the co-solvent. For the stretching vibrations between 4000 and 2500 cm^{-1}, a continuous decrease of the OH band is visible as long as the heat treatment is increased from 3 to 12 h. Similarly, the asymmetric and symmetric stretching vibrations of the CH_2 groups are progressively reduced and one can notice the absence of the asymmetric mode of CH_3 at 2963 cm^{-1} (by comparison with the $LiNb(OEt)_6$ precursor response) indicating that the initial ligand exchange is achieved between the primary ethoxy groups and a glycoxy chain only containing CH_2 units. This is also confirmed in the fingerprint region (Figure S21b, Supporting Information) where the characteristic skeletal modes of 1,5-pentanediol are comparable in the 1100–950 cm^{-1} range with the absorption bands of the transient solid species, showing a continuous release of the glycoxy ligands upon crystallization of LN. Note that a very similar trend is also observed when 1,4-butanediol is used as the co-solvent and that chemical modification of the lithium niobium ethoxide precursor with glycoxy groups is achieved as well (Figure S22, Supporting Information). Finally, The easier formation of the $LiNbO_3$ phase when primary alcohols are used as co-solvents is also illustrated in **Figure 7** after 6 h of solvothermal treatment at 235 °C by a direct comparison of the XRD patterns and FTIR spectra obtained after the addition of ethanol, butanol, 1,4-butanediol, 1,5-pentanediol, and 1,3-propanediol as co-solvent. If only the 6.5 Å transient phase is produced for the latter co-solvent, all samples prepared with glycols evidence a lower amount of LN nanocrystals and a significant contribution of the symmetric C—O stretching mode at ≈880 cm^{-1} and of the skeletal modes in the fingerprint region. In comparison with samples produced with ethanol and butanol as co-solvents, the high content of crystalline intermediates also demonstrates a measurable peak at 1640 cm^{-1} corresponding to the angular deformation of water and a residual contribution of the CH_2 scissoring mode at ≈1440 cm^{-1}.

Finally, the easy formation of LN nanocrystals under solvothermal conditions in comparison with calcination in air is addressed for a few co-solvents in Figure S23 (Supporting Information) through DTA/TG experiments. As the crystallization of the LN phase was observed to be less frustrated with primary alcohols of long carbon chains, a solvothermal treatment at 100 °C for 24 h was used to prepare the amorphous transient species for the heptanol and butanol cases. After washing and drying in air at 100 °C, their subsequent heating at 5 °C min^{-1} under argon first results in a poorly defined exothermic response in the 150–300 °C temperature range that we attribute to the slow crystallization of the 6.5 Å transient species. Note that a continuous and significant weight loss accounting for ≈5–8% of the initial powder mass is monitored below 400 °C from the TG traces. A

 © 2023 The Authors. Small published by Wiley-VCH GmbH

16136829, 0, Downloaded from https://onlinelibrary.wiley.com/doi/10.1002/smll.202306417 by Cochrane France, Wiley Online Library on [15/11/2023]. See the Terms and Conditions (https://onlinelibrary.wiley.com/terms-and-conditions) on Wiley Online Library for rules of use; OA articles are governed by the applicable Creative Commons License

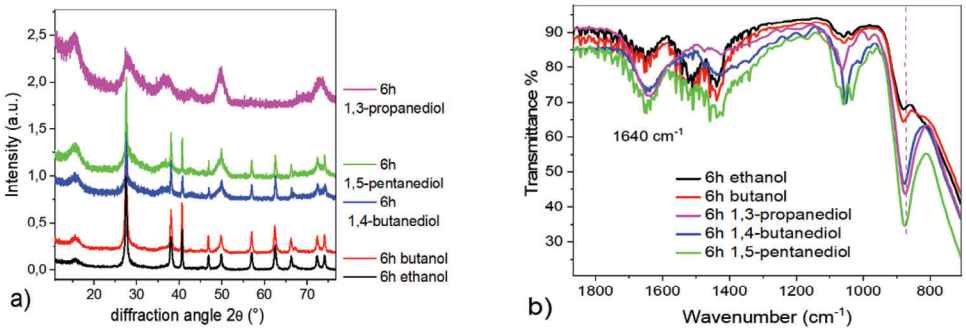

Figure 7. a) XRD diffraction patterns of samples produced at $h = 1.5$ with 2.25 mL of ethanol, butanol, 1,4-butanediol, 1,5-pentanediol, and 1,3-propanediol after a solvothermal treatment at 235 °C for 6 h, and b) corresponding FTIR spectra. The dashed line indicates the symmetric C–O stretching mode at ≈880 cm^{-1}.

second exothermic event, with a well-defined peak corresponding to the crystallization of LN, is then observed at 450 °C, i.e., at a much higher crystallization temperature by comparison with the solvothermal treatment. Interestingly, the same sequence of exothermic processes is measured for the 6.5 Å crystalline intermediates prepared with only ethanol at 200 °C for 3 h, and the absence of significant losses is also to be noticed upon crystallization of the LN phase above 480 °C. This would indicate that the 6.5 Å transient phase is not hydrated in agreement with the previously identified octanuclear complex of chemical composition $[Li_4Nb_4O_{10}(OEt)_4(EtOH)_{12}]$. Chemical analysis of the released gases was indeed performed from mass spectrometry coupled to DTA/TG experiments (Figure S23c,d, Supporting Information). Weight losses can be mainly attributed to water release through deshydroxylation in the 100–250°C temperature range. For these 6.5 Å crystalline intermediates prepared with only ethanol as solvent, crystallization of the $LiNbO_3$ phase at ≈480 °C is then concomitant with the departure of residual carbon species and thus in very good agreement with the aggregation-mediated crystallization mechanism discussed in the following section.

3. Discussion

Preparation of advanced nano- and hybrid-materials from the alkoxide route at low hydrolysis rates of the precursor solution is a well-established strategy for binary oxides. As an illustrative example, the rich chemistry of titanium-based oxo-clusters has been thoroughly investigated, leading to the identification of a large panel of possible stable or transient oligonuclear oxo-species.[54,55] Kinetically controlled hydrolysis and condensation reactions involved in the conventional sol-gel route, with silicon for instance, are not in fact responsible for the formation of the primary solid species with metal alkoxide precursors since a one-step hydrolysis-condensation is now admitted to first result in well-defined oligonuclear oxo-alkoxides and then in nuclei after their eventual coalescence.[56] Regarding pentavalent cations like niobium and tantalum, their respective ethoxide precursors $M(OEt)_5$ (M = Nb or Ta) have already been reacted with various chelating agents, thus, resulting in the formation of different coordination complexes corresponding to dinuclear, tetranuclear, and even octanuclear moieties in the case of Nb(V)[41] whereas several polynuclear core structures (Ta_5O_{18}, Ta_7O_{26}, and Ta_8O_{30}) have also been reported for Ta(V).[57] Regarding double metal alkoxides of Li, the number of identified complexes with pentavalent elements is comparatively low and, to our knowledge, only bimetallic moieties (giving $[LiNb(OEt)_6]_n$ chains with alternatively Li and Nb atoms) and tetranuclear species (with a heterocubane structure) have so far been produced and well-characterized.[47] In this work, we sought to identify both the molecular reaction pathway and crystallization mechanism leading to the formation of crystalline $LiNbO_3$ nanoparticles under solvothermal conditions after a systematic variation of the reaction medium composition with the addition of various co-solvents. A low hydrolysis rate of the precursor solution was also applied, with the aim to promote at room temperature, the formation of ideally, stoichiometric moieties already containing oxobridges and amorphous nuclei to shorten the usually required solvothermal treatment of 3–4 d at 220–240 °C. Time- and temperature-dependent measurements were also conducted to identify all the possible transient species before and after nucleation and upon heating.

Starting with separate precursors of lithium and niobium ethoxides, the formation of the expected $LiNb(OEt)_6$ dinuclear entity[39,40] was first attested from FTIR and NMR (Figure S1, Supporting Information) measurements. To avoid precipitation and to keep the reactive medium homogeneous upon hydrolysis, water diluted at 10 vol% in absolute ethanol[58] was then added, thus resulting in a rapid increase from ≈1 to 3 nm of the experimental DLS size distributions in volume. A DLS peak centered at 1 nm is consistent with the diameter of a $LiNb(OEt)_6$ unit calculated at 0.96 nm from the corresponding crystal structure[46] and the size of the $[LiNb(OEt)_8]^{2-}$ molecular entity (Figure S2, Supporting Information). On the other hand, the measured size at ≈3 nm cannot account for the diameter of the tetranuclear $[LiNbO(OEt)_4EtOH]_2$ complex derived at ≈1.5 nm from the crystalline cell of the bimetallic complex (Figure S3, Supporting Information).[59] This led us to further investigate this very qualitative size evolution monitored from standard DLS measurements with ESI–MS and NMR techniques. Before water addition, the main peaks observed in the 325–700 Da range are consistent with a mixture of the $LiNb(OEt)_6$ monomer and of the bimetallic lithium niobium oxoalkoxide $[LiNbO(OEt)_4EtOH]_2$ (Figure S3, Supporting Information) containing two Nb=O double bonds.[48] In the low mass region of Figure 1, peaks deriving from the tetranuclear complex were not really expected but we cannot exclude its partial formation

© 2023 The Authors. Small published by Wiley-VCH GmbH

16136829, 0, Downloaded from https://onlinelibrary.wiley.com/doi/10.1002/smll.202306417 by Cochrane France, Wiley Online Library on [15/11/2023]. See the Terms and Conditions (https://onlinelibrary.wiley.com/terms-and-conditions) on Wiley Online Library for rules of use; OA articles are governed by the applicable Creative Commons License

during the nebulization process. More interestingly, after hydrolysis has started at a low value of h fixed at 0.5 to prevent gel formation, ESI–MS experiments indicated the existence of a new mixed octanuclear complex made of $\{Li_4Nb_4O_{10}\}$ units and of composition $[Li_4Nb_4O_{10}(OEt)_4(EtOH)_{12}]$ (for neutral species), after assignments of all the experimental peaks only originating from ligand exchange with OH groups and partial fragmentation. To confirm the existence of such octanuclear complexes and the molecular reaction pathway leading to nonclassical nucleation of primary amorphous nuclei, nuclear magnetic resonance experiments were also conducted. The expected ligand exchange between the precursor ethoxy ligands and glycoxy groups once an excess of, for instance, 1,4-butanediol is added as a co-solvent was first assessed from the peak broadening and shifting of the Li resonance (Figure S1e, Supporting Information). After water addition, the immediate appearance of bulkier moieties corresponding to the octanuclear complexes was also evidenced by time-resolved ^{7}Li NMR spectra and DOSY experiments (Figure 1b; Figure S4, Supporting Information). For all tested co-solvents, note that the sequence of ligand exchange and oxocluster formation is also consistent with the visual change of the reactive medium upon hydrolysis (Figures S5 and S6, Supporting Information) and the more or less rapid formation of colloidal gels at room temperature. For simple alcohols of increasing carbon-chain length, high solvophobic interactions promote the rapid (<10 min) gel formation whereas the terminal OH of the glycoxy groups not only reduces these solvophobic interactions within the polar medium but also delays the appearance of the first amorphous nuclei after a slower aggregation of the transient mixed octanuclear complexes. This is particularly the case with 1,3-propandiol and to a less extent with 1,4-butanediol and 1,5-pentanediol since gelation was never observed for several hours after hydrolysis had been initiated at $h = 1.5$. We note here that ESI–MS and NMR experiments were not conducted for each tested co-solvent, either simple alcohol or glycol. Further experimental studies are thus needed to derive the exact chemical composition of all the possible heterometallic complexes and the exact structure of their corresponding octanuclear oxocluster. This work is however beyond the scope of the article. Crystallization of LN nanoparticles has already been shown to strongly depend on the annealing temperatures (Figures 3–5) and heating times (Figures 6a and 7a; Figures S15a, S18a, and S20a, Supporting Information) according to the co-solvent used. Besides, the initial ligand exchange occurring before hydrolysis has started is also in agreement with the time-resolved FTIR measurements indicating in the fingerprint domain a continuous decrease, with the increasing annealing time, of the characteristic skeletal C–C vibrations of the remaining surface glycoxy groups for the 1,4-butanediol and 1,5-pentanediol cases (Figures S21 and S22, Supporting Information). After 24 h of solvothermal treatments at 235 °C, representative FTIR spectra of dried LN nanocrystals are given in Figure S24 (Supporting Information) for several co-solvents. In the 400–800 cm^{-1} wavenumber range, the absorption modes observed at 440, 570, and 650 cm^{-1} are the optical signature of LN bulk crystals and powders after annealing at 1000 °C.[60] On the other hand, typical infrared vibrations of the alkoxy/glycoxy groups observed in the time-resolved studies are no longer present whereas a large band centered ≈3400 cm^{-1} can also be noticed. Its shape differs though from the well-known one arising from the OH^- impurity centers in congruent and stoichiometric bulk crystals grown from the Czochralski technique.[61] It is here attributed to the presence of surface OH groups leading to zeta potential values measured below −35 mV at neutral pH and thus the easy preparation of stable suspension in water or ethanol after gentle sonication of dried nanocrystal powders.

Regarding the crystallization mechanism and growth of primary LN nanocrystals, the amorphous nuclei obtained at room temperature in the colloidal gel after aggregation of the mixed octanuclear complexes have typical dimensions in the 5 nm size range according to SAXS experiments. Such features were also revealed from TEM imaging after a solvothermal treatment at 100 and 150 °C (Figures 2b,c and 5b; Figure S7b, Supporting Information) with different co-solvents. Contrary to the green and self-collection process leading to the room temperature formation of $BaTiO_3$ nanocrystals after hydrolysis of a mixture of the corresponding metal isopropoxides,[62] solvothermal treatment of the as-obtained viscous clear gel is here necessary since the temperature-resolved experiments (Figures 2 and 5a; Figure S13a, Supporting Information) demonstrate no crystallization of the LN phase and 6.5 Å intermediates below 150 °C. After 24 h at 235 °C, the formation of a monolith (**Figure 8**a) was however, systematically observed, which led us to further investigate this self-assembly process by paying special attention to the butanol and 1,4-butanediol co-solvents, both corresponding to two organic chains with four carbon atoms. A significant difference is indeed observed in the mean nanocrystal sizes derived along the [012], [110], and [006] directions (Figure S11, Supporting Information) while, according to the time-resolved studies, a higher content of the 6.5 Å crystalline intermediates is also clearly observed after 6 h with the glycols comparatively to the primary alcohols (Figure 7a). The easier formation of the $LiNbO_3$ phase with butanol is also noticeable from the TEM images of samples produced at $h = 1.5$ after a solvothermal treatment at 235 °C for only 3 and 6 h (Figure 8b,c). Small hybrid aggregates containing sub-10 nm nanocrystals of the 6.5 Å transient phase are first observed at 3 h, while after 6 h, primary LN nanocrystals with well-defined facets are already present together with the remaining crystalline intermediates. On the contrary, with 1,4-butanediol, samples produced after 6 h not only reveal from XRD patterns a smaller content of LN nanocrystals (Figure 7) but also in the TEM images of Figure 8d,e, larger hybrid aggregates in the 50–100 nm size range that latter transform, after 9 h, into primary LN nanocrystals of similar dimensions. Refinements of the XRD patterns also confirm this trend since the mean nanocrystal size obtained from the (012) reflection is calculated for the butanol case at 12, 13, 15, and 16 nm after 3, 6, 9, and 12 h of solvothermal treatment, respectively. Comparatively, the S_{012} mean size with 1,4-butanediol is estimated at 36, 68, and 74 nm after 6, 9, and 12 h.

Formation of the LN phase thus results from a more or less frustrated aggregation-mediated crystallization process within aggregates of variable sizes containing the 6.5 Å intermediates. In the literature, this mechanism has already been intensively discussed for centrosymmetric oxide materials (sulfates, carbonates, etc.) and bioinspired routes.[6,7,9,10,63] Organic–inorganic interactions between organic additives and the primary solid intermediates, together with the initial content of

© 2023 The Authors. Small published by Wiley-VCH GmbH

16136829, 0, Downloaded from https://onlinelibrary.wiley.com/doi/10.1002/smll.202306417 by Cochrane France, Wiley Online Library on [15/11/2023]. See the Terms and Conditions (https://onlinelibrary.wiley.com/terms-and-conditions) on Wiley Online Library for rules of use; OA articles are governed by the applicable Creative Commons License

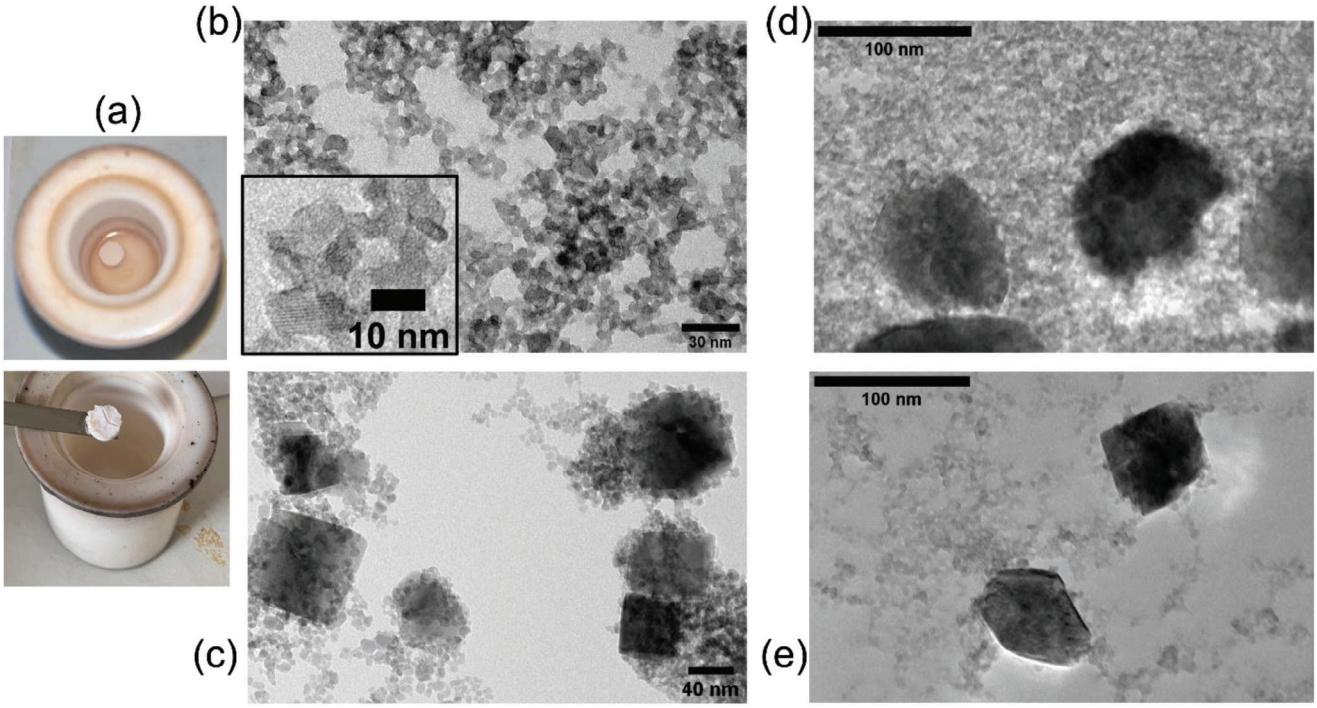

Figure 8. a) Typical photo images of a monolith after a solvothermal treatment for 24 h at 235 °C and representative TEM images of samples produced at $h = 1.5$ with 2.25 mL of butanol after a solvothermal treatment at 235 °C for 3 h (b) and 6 h (c), and with 2.25 mL of 1,4-butanediol for 9 h (d) and 12 h (e). Aggregates of the 6.5 Å crystalline intermediates are highlighted in the inset of (b).

water/surfactants in microemulsion-based systems, are known to play a key role in the overall formation mechanism and final composition/morphology of the as-prepared ternary oxides. Note that for polar NCO nanomaterials, surface-anchored ligands, and physical fields may also result in a 3D alignment and ordered nanocrystal superstructures, or mesocrystals, as already evidenced for several titanate and (K, Na)NbO_3 compounds.[64] For $LiNbO_3$, ordered sheaf-like morphologies have been observed from sub-10 nm seeds stabilized by triphenylphosphine oxide ligands[65] whereas disordered spherical hybrid aggregates, i.e., with no 3D alignment of the nanocrystals, have also been recently produced.[20,21] In our studies, such morphologies have only been noticed when 1,2-ethanediol was used as the co-solvent (Figure S25, Supporting Information) resulting in micrometer aggregates containing phase pure LN nanocrystals of 20 nm. According to FTIR measurements, a lower contribution of the OH band at ≈3400 cm^{-1} and the stronger intensity of the asymmetric C–O vibrations at ≈1100 cm^{-1} are noticeable with 1,2-ethanediol, comparatively to the ethanol case. The higher content of remaining surface organic ligands with 1,2-ethanediol could explain the self-assembly of hybrid aggregates. It also confirms that glycols with short carbon-chain lengths are less prone to yield suspensions of non-aggregated LN nanocrystals and that binding interactions of the organic ligands to the inorganic core of the crystalline intermediates are responsible for the final LN nanocrystal size and aggregation degree. Mesoscale transformations implying rearrangements of the surface-anchored organic molecules within the transient loosely-packed amorphous or crystalline intermediates are indeed known to either result in complex hybrid superstructures or in individual nanocrystals.[10] Such rearrangement of the organic layer and final removal of the surface-anchored alkoxy/glycoxy groups can here be simply interpreted in terms of the Nb–OR binding interaction. The energy of the Nb–OR bond indeed depends on the electron-donor inductive effect of the carbon-chain atoms. Long chains increase the negative charge of the oxygen atom thus reducing the core-ligand interactions and promoting the subsequent release of RO^- alkoxy moieties. Their reaction with water, initially added in slight excess compared to the number of the precursor ethoxy groups, results in the surface hydroxyl groups evidenced from FTIR studies and minimal byproduct content since the primary alcohols initially added as co-solvent are finally retrieved in the liquid phase surrounding the final monolith. Such a self-collection synthesis can be seen as a relatively green process since intensive centrifugation/separation steps are not needed to get a high yield of nanocrystals with little waste since the initial mixture of solvents is restored and recyclable. Very notably, inductive effects that are known to increase with the chain length from the first till the fourth carbon atom of an alkyl group,[66,67] account for the continuous decrease of the final nanocrystal size with the primary alcohols ranging from ethanol to butanol while almost no size variation is monitored for pentanol, hexanol, and heptanol (Figure 3b). When glycols are added as the co-solvent, the terminal OH of the glycoxy pendant chain strongly decreases the inductive effects on the Nb–OR bond, as illustrated in **Figure 9** where the main findings of this study are also summarized with a special focus on the butanol and 1,4-butanediol cases. For this latter, rearrangements of the organic layer within primary hydride aggregates of bigger size are less favorable since the removal of the RO^- glycoxy moieties is

 © 2023 The Authors. Small published by Wiley-VCH GmbH

16136829, 0, Downloaded from https://onlinelibrary.wiley.com/doi/10.1002/smll.202306417 by Cochrane France, Wiley Online Library on [15/11/2023]. See the Terms and Conditions (https://onlinelibrary.wiley.com/terms-and-conditions) on Wiley Online Library for rules of use; OA articles are governed by the applicable Creative Commons License

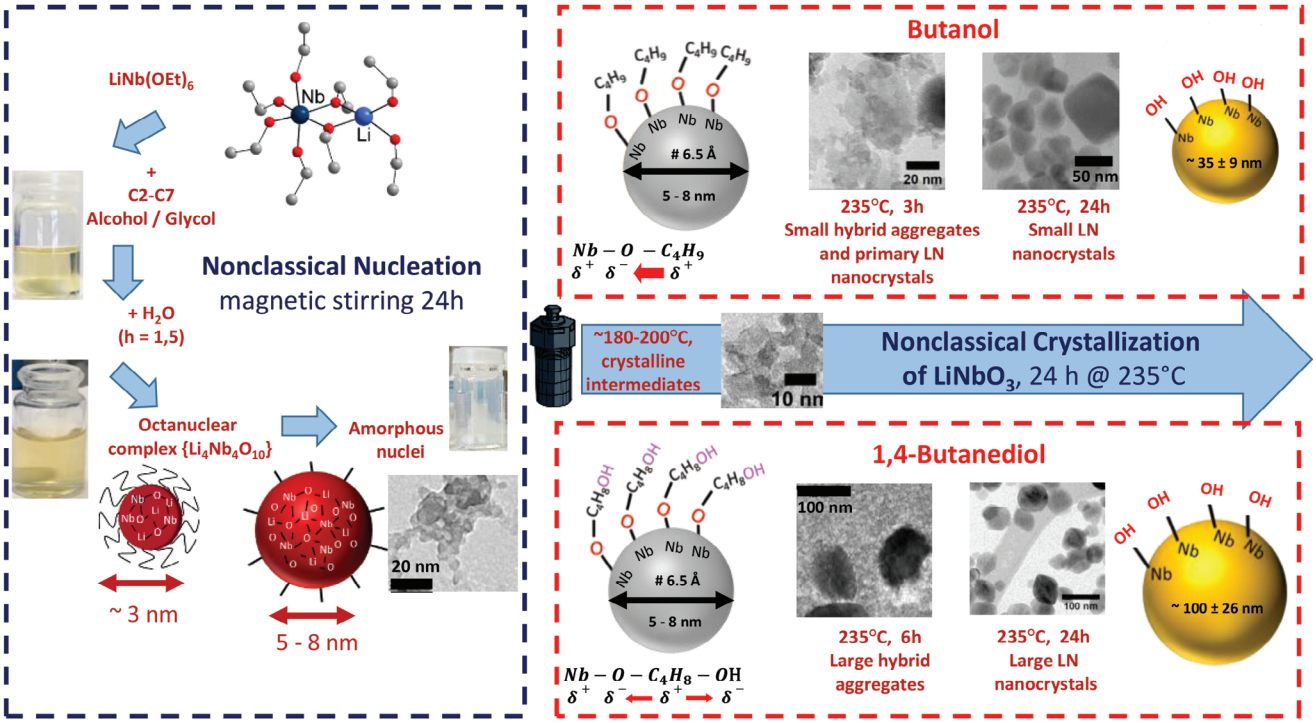

Figure 9. Overview of the nonclassical nucleation scheme and aggregation-mediated crystallization process with a special focus on the butanol and 1,4-butanediol co-solvents. Upon heating, two schematic representations of the corresponding 6.5 Å crystalline intermediates are given on the left side of the dash-red rectangles, with an emphasis on the surface linear ligand containing four carbon atoms in each case. The electron-donor inductive effect produced on the oxygen atom bonded to Nb, represented by a red arrow of varying amplitude according to its intensity, is weaker with a terminal OH group.

required and, finally, crystallization of the LN phase is frustrated. The resulting nanocrystal size is significantly larger as outlined in Figure S11 (Supporting Information) for all the co-solvents leading to non-aggregated nanoparticles after re-dispersion in ethanol. More specifically, replacing butanol from 1,4-butanediol results in a size increase from ≈35 to ≈100 nm according to the size distribution histograms of Figures 3 and 4. A decrease in the nanocrystal shape anisotropy factor (S_{110}/S_{006}) can also be noticed from the results of the XRD refinements depicted in Figure S11 (Supporting Information). Although the accuracy of the derived crystallite size is only indicative above 50 nm, the shape anisotropy is reduced from ≈2.8 with butanol to ≈1.4 by 1,4-butanediol. If rod- and plate-like morphologies are known to result from cooperative mesoscale transformations,[9,10] crystallization of the LN phase is here accompanied by the built-up of a polar order and thus higher Nb–OR binding interactions for Nb atoms belonging to the positively-charged (001) plane. As the crystallization of LN is observed to occur below 200 °C with butanol (and all primary alcohols) and above 200 °C for 1,4-butanediol (Figure 5a), the temperature-induced rearrangements within hybrid aggregates and the associated release of the RO^- glycoxy moieties is less sensitive to the spontaneous polarization at higher thermal energy. This leads to less anisotropic nanocrystals when glycols are used as co-solvent. We also note from the DTA traces of Figure S23 (Supporting information) and the second exothermic peak at 450 °C, the expected higher thermodynamic stability of LN nanocrystals comparatively to the 6.5 Å intermediates during the aggregation-mediated crystallization of $LiNbO_3$. After its occurrence, a mechanism of attachment and surface recrystallization[6] of the remaining low amount of crystalline intermediates is involved at the surface of the primary LN nanocrystals (Figures S19 and S20d–h, Supporting Information) thus leading, with or almost all the co-solvents tested, to single phase $LiNbO_3$ nanomaterials after only 24 h of solvothermal treatment.

4. Conclusion

After a systematic variation of the reactive medium composition combined with extensive time- and temperature-resolved experiments, we elucidate the entire growth process of $LiNbO_3$ nanocrystals from the aqueous alkoxide route under solvothermal conditions. A nonclassical nucleation scheme involving the rapid formation, at room-temperature, of oxoclusters with a $\{Li_4Nb_4O_{10}\}$ core and their aggregation into a colloidal gel composed of 5 nm amorphous nuclei is first demonstrated. Solvophobic interactions between the oxocluster pendant chains and the reactive medium mediate this process. Further aggregation is observed upon heating with syneresis of the colloidal gel and monolith formation. Crystallization of the LN phase is then governed by the variable Nb–OR binding interactions associated with the nature and carbon-chain length of the surface alkoxy/glycoxy groups within hybrid aggregates containing sub-10 nm crystalline intermediates. If work is still in progress to further reduce the final size- and shape-distributions of the as-obtained $LiNbO_3$ nanocrystals by paying attention to the hydrolysis rate and

© 2023 The Authors. Small published by Wiley-VCH GmbH

16136829, 0, Downloaded from https://onlinelibrary.wiley.com/doi/10.1002/smll.202306417 by Cochrane France, Wiley Online Library on [15/11/2023]. See the Terms and Conditions (https://onlinelibrary.wiley.com/terms-and-conditions) on Wiley Online Library for rules of use; OA articles are governed by the applicable Creative Commons License

stirring conditions at room temperature, this green chemistry approach and extensive experimental study allowing identification of all the transient species give new insights into the detailed formation mechanisms of functional non-centrosymmetric metal-oxide nanoparticles from standard alkoxide precursors.

5. Experimental Section

Chemicals and Synthesis of $LiNbO_3$ Nanocrystals: Ethoxides of niobium ($Nb(OCH_2CH_3)_5$, 99.95% trace metal basis) and lithium ($LiOCH_2CH_3$, at 1.0 M in ethanol) were both purchased from Sigma–Aldrich and stored under argon because of their high degree of reactivity with air which is known to alter the formation of $LiNbO_3$ nanocrystals.[25] Co-solvents including primary alcohols of increasing chain length from absolute ethanol to heptanol, secondary alcohols from 2-propanol to 2-heptanol (with the exception of 2-hexanol), and glycols from 1,2-ethanediol to 1,7-heptanediol (with the exception of 1,6-hexanediol which is solid at room temperature) were provided by Sigma–Aldrich or Fischer Scientific. All solvents of reagent grade were used as received without further purification.

Solvothermal preparation of lithium niobate ($LiNbO_3$) nanocrystals in a 23 mL Teflon-lined stainless-steel autoclave (Parr Instruments Co., Moline, IL, USA) was performed at 235 °C for 1 d unless specified in the text for the time- and temperature-resolved experiments. In a typical synthesis, niobium ethoxide (154 µL, 0.6 mmol) was first diluted under argon in 3.75 mL of absolute ethanol before the addition of lithium ethoxide (600 µL, 0.6 mmol) thus yielding the bimetallic lithium niobium ethoxide $LiNb(OCH_2CH_3)_6$ at 0.133 M in ethanol.[40,46] Homogenization with magnetic stirring for ≈5 min was then carried outside the glove box resulting in a transparent yellow solution.

A systematic variation of the reactive medium composition was achieved after the addition under stirring of 2.25 mL of co-solvent resulting in ligand exchange with the ethoxy groups. To promote condensation and to sensibly shorten the minimum reaction times of 3–4 d as recently observed for the preparation under solvothermal conditions of well-crystallized LN nanoparticles from the alkoxide route,[18–22,25] a mixture of 100 µL of distilled water and 900 µL of absolute ethanol was then added dropwise thus keeping an homogeneous solution without precipitation.[39,58] The reaction medium was then kept under vigorous stirring for 24 h before the solvothermal treatment at 235 °C for only 1 d. For each synthesis, the final solution volume was fixed at 7.75 mL to keep almost constant the autogenous pressure within the autoclave. After cooling down to room temperature, the monolith typically obtained was isolated from the reaction medium upon centrifugation (13 500 rpm) before being re-dispersed twice in ethanol for additional washing and centrifugation. After drying at 100 °C for 1–2 h, the expected mass of LN nanocrystals at ≈90 mg could be easily dispersed under sonication to prepare colloidal suspensions.

Characterizations: XRD patterns were obtained in the 5–120° 2θ range with the Co Kα_1 and Kα_2 radiations of a PANalytical X'Pert^3 powder diffractometer (Malvern Panalytical, Palaiseau, France) equipped with a rotating zero-background silicon sample holder. The apparent nanocrystal size S_{hlk} derived from the peak broadening along each (hkl) direction was calculated after extraction of the integrated intensities within FullProf according to the Le Bail global fitting procedure. A pseudo-Voigt function and a platelet morphology were assumed to fit the anisotropic broadening of the diffraction peaks with consideration of the Lorentzian and Gaussian parts in the FWHM and after careful assessment of the instrument resolution from a Silicon calibration powder.

SAXS measurements were performed with another PANalytical X'Pert^3 powder diffractometer (40 mA, 45 kV) equipped with a copper anode and a 1D Pixel detector. The angular range is set between −0.11° and 5.00° for an exposure time of 1 s per step size fixed at 0.01°. In the data treatment carried out with the EasySAXS interface, the scattering vector q was typically fixed between 0.07 and 1.50 nm^{-1}. Spectra were all corrected from the background signal measured from two mylar sheets used as the sample holder containing the gels or powders extracted at various aging times. The scattering intensity $I_p(q,R)$ was fitted with the form factor of homogeneous spherical particles of radius R given in Equation (1)

$$\frac{3(\sin qR - qR\cos qR)}{(qR)^3} \tag{1}$$

DLS (Zetasizer Nano ZS, Malvern Panalytical, Palaiseau, France) was used to qualitatively investigate the first steps of the condensation process after the addition of water in the initial alkoxide solution. ESI–MS (or HRMS(ESI)) measurements were performed from an Exploris 240 instrument (direct injection, Thermofisher) equipped with an LTQ-Orbitrap analyzer and a nanochip-based ESI for ionization. Samples were diluted by a factor of 10 000 in EtOH before injection.

^{7}Li and ^{93}Nb NMR spectra were acquired at 298 K on a Bruker AV4 spectrometer (^{1}H: 400.1 Mhz, ^{7}Li: 155.4 MHz, ^{93}Nb: 97.8 MHz) equipped with a 5 mm BBO probe capable of generating gradient field strength of 54 G cm^{-1} and without deuterated lock solvent (i.e., unlocked). Prior to the acquisition, the spectrometer was pre-locked and pre-shimmed on a line shape standard (3% $CHCl_3$ in acetone-d6). ^{7}Li Spectra were acquired with 64 30° pulses of 4.16 µs, a spectral width of 4.7 kHz, an acquisition time of 3.4 s, and a preparation delay (d1) of 1 s. The free induction decays (32k points) were zero-filled to 64k points and multiplied by a 0.3 Hz exponential line-broadening function prior to Fourier transformation to the frequency domain.

^{93}Nb Spectra were acquired with 512 30° pulses of 3.3 µs, a spectral width of 100 kHz, an acquisition time of 0.17 s, a preparation delay (d1) of 0.1 s. The free induction decays (32k points) were zero-filled to 64k points and multiplied by a 100 Hz exponential line-broadening function prior to Fourier transformation to the frequency domain. ^{7}Li DOSY experiments were performed with the Bruker DOSY pulse sequence (ledbpgp2s). The DOSY diffusion time interval (d20) and gradient pulse length (p30) were set at 0.1 s and 2200 ms, respectively, with a recycle delay (d1) of 0.1 s and an acquisition time (aq) of 1.7 s. Each 1D free induction decay had 16k complex points. The diffusion gradients were ramped from 2% to 98% of the maximal gradient field strength of the probe at linear increments to generate 32 increments in the diffusion dimension. DOSY NMR data processing was performed using Bruker Topspin software.

Transmission electron microscopy (TEM) images from a JEOL 2100 HT apparatus operating at 200 kV (JEOL Europe SAS, Croissy Sur Seine, France) were acquired to further estimate the final mean nanocrystal size and size distribution. Size histograms were obtained from the surface analysis of at least 100 nanocrystals by assuming a disk-shaped morphology. SAED patterns and EDS spectra were also recorded to further analyze the structures and chemical compositions of all transient solid species. Fourier Transform Infra-Red spectroscopy (FTIR) measurements were performed from a Shimadzu (IRAffinity-1, Shimadzu France, Marne-la-Vallée) spectrometer within the attenuated-total-reflection configuration. Differential thermal and thermogravimetric analyses (DTA-TG) were carried out with a SETARAM TAG 16 equipment, using 30 mg of powder within 100 µL alumina crucible, at a heating rate of 10 °C min^{-1} under either pure Ar or Ar/O_2 (80/20) atmosphere. Chemical analysis of the gaseous by-products was done from a coupled HIDEN analytical apparatus (QGA-HAL201-RC) mass spectrometer.

Supporting Information

Supporting Information is available from the Wiley Online Library or from the author.

Acknowledgements

This work was supported by the French Agence Nationale de la Recherche (projects RACINE, ANR-17-CE24-0029-03, and DARE, ANR-21-CE09-0036-01), the French-Swiss Interreg V program (project OncoNanoscreen), and the Swiss National Science Foundation (DARE, grant 200021E_205754).

© 2023 The Authors. Small published by Wiley-VCH GmbH

16136829, 0, Downloaded from https://onlinelibrary.wiley.com/doi/10.1002/smll.202306417 by Cochrane France, Wiley Online Library on [15/11/2023]. See the Terms and Conditions (https://onlinelibrary.wiley.com/terms-and-conditions) on Wiley Online Library for rules of use; OA articles are governed by the applicable Creative Commons License

The authors also want to kindly thank Mathias Urbain and several undergraduate students including Naglis Gasuinas and Amen Bou Ali for their involvement during their stay in the SYMME laboratory. N. Blanchard and the Centre Lyonnais de Microscopie (CLYM) platform are thanked for their help with TEM experiments. The authors also thank the ISIC Mass Spectrometry and Elemental Analysis Platform for mass spectrometry measurements.

Conflict of Interest

The authors declare no conflict of interest.

Data Availability Statement

The data that support the findings of this study are available from the corresponding author upon reasonable request.

Keywords

aqueous alkoxide route, crystallization mechanism, $LiNbO_3$ nanocrystals, nonclassical nucleation

Received: July 28, 2023
Revised: October 9, 2023
Published online:

[1] N. D. Loh, S. Sen, M. Bosman, S. F. Tan, J. Zhong, C. A. Nijhuis, P. Král, P. Matsudaira, U. Mirsaidov, *Nat. Chem.* **2017**, *9*, 77.
[2] A. Lassenberger, T. A. Grünewald, P. D. J. Van Oostrum, H. Rennhofer, H. Amenitsch, R. Zirbs, H. C. Lichtenegger, E. Reimhult, *Chem. Mater.* **2017**, *29*, 4511.
[3] H. Chang, B. H. Kim, H. Y. Jeong, J. H. Moon, M. Park, K. Shin, S. I. Chae, J. Lee, T. Kang, B. K. Choi, J. Yang, M. S. Bootharaju, H. Song, S. H. An, K. M. Park, J. Y. Oh, H. Lee, M. S. Kim, J. Park, T. Hyeon, *J. Am. Chem. Soc.* **2019**, *141*, 7037.
[4] D. Gebauer, H. Cölfen, *Nano Today* **2011**, *6*, 564.
[5] M. Liu, K. Wang, L. Wang, S. Han, H. Fan, N. Rowell, J. A. Ripmeester, R. Renoud, F. Bian, J. Zeng, K. Yu, *Nat. Commun.* **2017**, *8*, 15467.
[6] J. J. De Yoreo, P. U. P. A. Gilbert, N. A. J. M. Sommerdijk, R. L. Penn, S. Whitelam, D. Joester, H. Zhang, J. D. Rimer, A. Navrotsky, J. F. Banfield, A. F. Wallace, F. M. Michel, F. C. Meldrum, H. Cölfen, P. M. Dove, *Science* **2015**, *349*, aaa6760.
[7] J. Lee, J. Yang, S. G. Kwon, T. Hyeon, *Nat. Rev. Mater.* **2016**, *1*, 16034.
[8] N. T. K. Thanh, N. Maclean, S. Mahiddine, *Chem. Rev.* **2014**, *114*, 7610.
[9] S. Mann, *Nat. Mater.* **2009**, *8*, 781.
[10] H. Cölfen, S. Mann, *Angew. Chem., Int. Ed.* **2003**, *42*, 2350.
[11] G. Dantelle, S. Beauquis, R. Le Dantec, V. Monnier, C. Galez, Y. Mugnier, *Small* **2022**, *18*, 2200992.
[12] M. Kakihana, *J. Sol–Gel Sci. Technol.* **1996**, *6*, 7.
[13] A. E. Danks, S. R. Hall, Z. Schnepp, *Mater. Horiz.* **2016**, *3*, 91.
[14] S. Mishra, S. Daniele, *Chemistry* **2020**, *26*, 9292.
[15] D. R. Modeshia, R. I. Walton, *Chem. Soc. Rev.* **2010**, *39*, 4303.
[16] S. H. Feng, G. H. Li, in *Modern Inorganic Synthetic Chemistry*, Elsevier, Amsterdam **2017**, pp. 73–104.
[17] M. Niederberger, N. Pinna, J. Polleux, M. Antonietti, *Angew. Chem., Int. Ed.* **2004**, *43*, 2270.
[18] R. F. Ali, B. D. Gates, *Chem. Mater.* **2018**, *30*, 2028.
[19] R. F. Ali, M. Bilton, B. D. Gates, *Nanoscale Adv.* **2019**, *1*, 2268.
[20] R. F. Ali, B. D. Gates, *Nanoscale* **2021**, *13*, 3214.
[21] R. F. Ali, B. D. Gates, *RSC Adv.* **2022**, *12*, 822.
[22] D. Mohanty, G. S. Chaubey, A. Yourdkhani, S. Adireddy, G. Caruntu, J. B. Wiley, *RSC Adv.* **2012**, *2*, 1913.
[23] J. Livage, M. Henry, J. P. Jolivet, C. Sanchez, *MRS Bull.* **1990**, *15*, 18.
[24] M. Nabavi, S. Doeuff, C. Sanchez, J. Livage, *J. Non-Cryst. Solids* **1990**, *121*, 31.
[25] M. Urbain, F. Riporto, S. Beauquis, V. Monnier, J. C. Marty, C. Galez, C. Durand, Y. Chevolot, R. L. Dantec, Y. Mugnier, *Nanomaterials* **2021**, *11*, 154.
[26] P. Pantazis, J. Maloney, D. Wu, S. E. Fraser, *Proc. Natl. Acad. Sci. USA* **2010**, *107*, 14535.
[27] D. Staedler, T. Magouroux, R. Hadji, C. Joulaud, J. Extermann, S. Schwung, S. Passemard, C. Kasparian, G. Clarke, M. Gerrmann, R. Le Dantec, Y. Mugnier, D. Rytz, D. Ciepielewski, C. Galez, S. Gerber-Lemaire, L. Juillerat-Jeanneret, L. Bonacina, J. P. Wolf, *ACS Nano* **2012**, *6*, 2542.
[28] J. Riporto, A. Demierre, V. Kilin, T. Balciunas, C. Schmidt, G. Campargue, M. Urbain, A. Baltuska, R. L. Dantec, J. P. Wolf, Y. Mugnier, L. Bonacina, *Nanoscale* **2018**, *10*, 8146.
[29] G. Campargue, L. L. Volpe, G. Giardina, G. Gaulier, F. Lucarini, I. Gautschi, R. L. Dantec, D. Staedler, D. Diviani, Y. Mugnier, J. P. Wolf, L. Bonacina, *Nano Lett.* **2020**, *20*, 8725.
[30] L. L. Xuan, C. Zhou, A. Slablab, D. Chauvat, C. Tard, S. Perruchas, T. Gacoin, P. Villeval, J. F. Roch, *Small* **2008**, *4*, 1332.
[31] J. Extermann, L. Bonacina, E. Cuña, C. Kasparian, Y. Mugnier, T. Feurer, J. P. Wolf, *Opt. Express* **2009**, *17*, 15342.
[32] L. Dubreil, I. Leroux, M. Ledevin, C. Schleder, L. Lagalice, C. Lovo, R. Fleurisson, S. Passemard, V. Kilin, S. Gerber-Lemaire, M. A. Colle, L. Bonacina, K. Rouger, *ACS Nano* **2017**, *11*, 6672.
[33] G. Malkinson, P. Mahou, É. Chaudan, T. Gacoin, A. Y. Sonay, P. Pantazis, E. Beaurepaire, W. Supatto, *ACS Photonics* **2020**, *7*, 1036.
[34] L. Vittadello, J. Klenen, K. Koempe, L. Kocsor, Z. Szaller, M. Imlau, *Nanomaterials* **2021**, *11*, 3193.
[35] R. F. Ali, I. Guo, H. Kang, M. J. Radford, D. T. Yapp, B. D. Gates, *Langmuir* **2021**, *37*, 7689.
[36] R. De Matos, A. Gheata, G. Campargue, J. Vuilleumier, L. Nicolle, K. Pierzchala, I. Jelescu, F. Lucarini, I. Gautschi, F. Riporto, R. L. Dantec, Y. Mugnier, A. S. Chauvin, M. Mazzanti, D. Staedler, D. Diviani, L. Bonacina, S. Gerber-Lemaire, *ACS Appl. Nano Mater.* **2022**, *5*, 2912.
[37] J. Vuilleumier, G. Gaulier, R. De Matos, Y. Mugnier, G. Campargue, J. P. Wolf, L. Bonacina, S. Gerber-Lemaire, *Helv. Chim. Acta* **2020**, *103*, 1900251.
[38] A. Gheata, G. Gaulier, G. Campargue, J. Vuilleumier, S. Kaiser, I. Gautschi, F. Riporto, S. Beauquis, D. Staedler, D. Diviani, L. Bonacina, S. Gerber-Lemaire, *ACS Nanosci. Au* **2022**, *2*, 355.
[39] S. Hirano, K. Kato, *Solid State Ionics* **1989**, *32/33*, 765.
[40] D. Eichhorst, K. Howard, D. Payne, in *Ultrastructure Processing of Advanced Materials*, John Wiley, New York **1992**, pp. 87–93.
[41] D. Andriotou, S. Duval, C. Volkringer, X. Trivelli, W. E. Shepard, T. Loiseau, *Chemistry* **2022**, *28*, e202201464.
[42] D. C. Bradley, B. N. Chakravarti, W. Wardlaw, *J. Chem. Soc.* **1956**, 2381.
[43] A. J. Barnes, H. E. Hallam, *Trans. Faraday Soc.* **1970**, *66*, 1932.
[44] P. Griesmar, G. Papin, C. Sanchez, J. Livage, *Chem. Mater.* **1991**, *3*, 335.
[45] R. Azouani, A. Soloviev, M. Benmami, K. Chhor, J. F. Bocquet, A. Kanaev, *J. Phys. Chem. C* **2007**, *111*, 16243.
[46] D. J. Eichorst, K. E. Howard, D. A. Payne, S. R. Wilson, *Inorg. Chem.* **1990**, *29*, 1458.
[47] M. Mäntymäki, M. Ritala, M. Leskelä, *Coord. Chem. Rev.* **2012**, *256*, 854.
[48] E. P. Turevskaya, N. Y. Turova, A. V. Korolev, A. I. Yanovsky, Y. T. Struchkov, *Polyhedron* **1995**, *14*, 1531.
[49] S. Adireddy, C. Lin, B. Cao, W. Zhou, G. Caruntu, *Chem. Mater.* **2010**, *22*, 1946.

 © 2023 The Authors. Small published by Wiley-VCH GmbH

16136829, 0, Downloaded from https://onlinelibrary.wiley.com/doi/10.1002/smll.202306417 by Cochrane France, Wiley Online Library on [15/11/2023]. See the Terms and Conditions (https://onlinelibrary.wiley.com/terms-and-conditions) on Wiley Online Library for rules of use; OA articles are governed by the applicable Creative Commons License

[50] D. Caruntu, T. Rostamzadeh, T. Costanzo, S. Salemizadeh Parizi, G. Caruntu, *Nanoscale* **2015**, *7*, 12955.
[51] M. Rajamathi, R. Seshadri, *Curr. Opin. Solid State Mat. Sci.* **2002**, *6*, 337.
[52] M. Nyman, T. M. Anderson, P. P. Provencio, *Cryst. Growth Des.* **2009**, *9*, 1036.
[53] S. L. Skjærvø, G. K. Ong, O. G. Grendal, K. H. Wells, W. Van Beek, K. Ohara, D. J. Milliron, S. Tominaka, T. Grande, M. A. Einarsrud, *Inorg. Chem.* **2021**, *60*, 7632.
[54] C. Sanchez, G. J. D. A. A. Soler-Illia, F. Ribot, T. Lalot, C. R. Mayer, V. Cabuil, *Chem. Mater.* **2001**, *13*, 3061.
[55] L. Rozes, C. Sanchez, *Chem. Soc. Rev.* **2011**, *40*, 1006.
[56] V. G. Kessler, *J. Sol-Gel Sci. Technol.* **2009**, *51*, 264.
[57] I. Abrahams, D. C. Bradley, H. Chudzynska, M. Motevalli, P. O'Shaughnessy, *J. Chem. Soc. Dalton Trans.* **2000**, 2685.
[58] S. I. Hirano, K. Kato, *Adv. Ceram. Mat.* **1987**, *2*, 142.
[59] A. Yanovskij, E. Turevskaya, N. Y. Turova, Y. T. Struchkov, *Koord. Khim.* **1985**, *11*, 110.
[60] H. C. Zeng, S. K. Tung, *Chem. Mater.* **1996**, *8*, 2667.
[61] M. Y. Salloum, O. S. Grunsky, A. A. Man'shina, A. S. Tver'yanovich, Y. S. Tver'yanovich, *Russ. Chem. Bull.* **2009**, *58*, 2228.
[62] S. Liu, L. Huang, W. Li, X. Liu, S. Jing, J. Li, S. O'brien, *Nanoscale* **2015**, *7*, 11766.
[63] F. C. Meldrum, H. Cölfen, *Chem. Rev.* **2008**, *108*, 4332.
[64] R.-Q. Song, H. Cölfen, *Adv. Mater.* **2010**, *22*, 1301.
[65] B. D. Wood, V. Mocanu, B. D. Gates, *Adv. Mater.* **2008**, *20*, 4552.
[66] R. W. Holman, **1995**.
[67] R. Tandon, T. A. Nigst, H. Zipse, *Eur. J. Org. Chem.* **2013**, *2013*, 5423.

 © 2023 The Authors. Small published by Wiley-VCH GmbH

16136829, 0, Downloaded from https://onlinelibrary.wiley.com/doi/10.1002/smll.202306417 by Cochrane France, Wiley Online Library on [15/11/2023]. See the Terms and Conditions (https://onlinelibrary.wiley.com/terms-and-conditions) on Wiley Online Library for rules of use; OA articles are governed by the applicable Creative Commons License